Inorganic Chemistry

pubs.acs.org/IC

Article

Molecules versus Nanoparticles: Identifying a Reactive Molecular Intermediate in the Synthesis of Ternary Coinage Metal Chalcogenides

Sweta Gahlot, Erwann Jeanneau, Deobrat Singh, Pritam Kumar Panda, Yogendra Kumar Mishra, Rajeev Ahuja, Gilles Ledoux, and Shashank Mishra*

Cite This: https://dx.doi.org/10.1021/acs.inorgchem.0c00758

Read Online

ACCESS | Metrics & More | Article Recommendations | Supporting Information

ABSTRACT: The identification of reactive intermediates during molecule-to-nanoparticle (NP) transformation has great significance in comprehending the mechanism of NP formation and, therefore, optimizing the synthetic conditions and properties of the formed products. We report here the room temperature (RT) synthesis of AgCuSe NPs from the reaction of di-*tert*-butyl selenide with trifluoroacetates (TFA) of silver(I) and copper(II). The isolation and characterization of a molecular species during the course of this reaction, $[Ag_2Cu(TFA)_4(^tBu_2Se)_4]$ (**1**), which shows extraordinary reactivity and interesting thermochromic behavior (blue at 0 °C and green at RT), confirmed that ternary metal selenide NPs are formed via this intermediate species. Similar reactions with related dialkyl chalcogenide R_2E resulted in the isolation of molecular species of similar composition, $[Ag_2Cu(TFA)_4(R_2E)_4]$ [R = ^{t}Bu, E = S (**2**); R = Me, E = Se (**3**); R = Me, E = S (**4**)], which are stable at RT but can be converted to ternary metal chalcogenides at elevated temperature. Density functional theory calculations confirm the kinetic instability of **1** and throw light on its thermochromic properties.

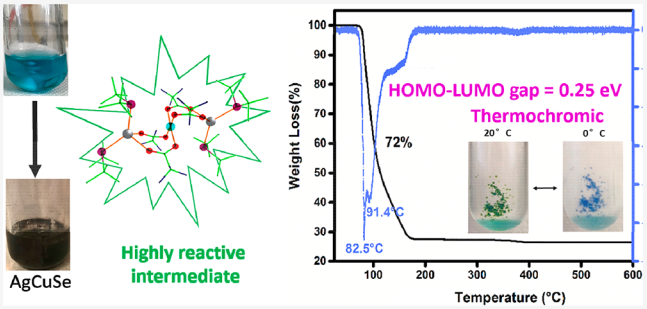

INTRODUCTION

The coinage metal chalcogenide nanomaterials are currently under intense investigations for their various physical properties (low band gaps of 0.15−2.0 eV, low toxicity compared to lead- and cadmium-containing chalcogenides, high absorption coefficients, near-IR emission, etc.) and widespread applications (thermoelectrics, photovoltaic solar cells, photocatalysis, memory devices, nonlinear optics, energy storage, etc.).[1,2] In particular, the ternary silver−copper chalcogenides, which have structures that favor high mobility of the ions, are fast emerging as interesting materials for applications in thermoelectricity, photocatalysis, and electrochemical devices (batteries, fuel cells, gas sensors, etc.).[3−6] Among these, AgCuSe exists in two phases: a room-temperature (RT) β-AgCuSe phase having an orthorhombic structure and a high-temperature α-AgCuSe phase with a cubic structure.[3,4] The structure of β-phase consists of alternating layers of Ag and CuSe, whereas the high-temperature α-phase is composed of Ag^+ and Cu^+ cations randomly distributed at tetrahedral sites of the face-centered-cubic unit cell of selenium atoms. The RT structure of Ag_3CuS_2 is similar to that of Ag_2S and contains silver ions in two different environments, i.e., octahedral and highly distorted tetrahedral. The copper atoms are linearly coordinated by two sulfur atoms and bridge the channels.[7] Although the nanometric forms of ternary metal chalcogenides have previously been synthesized by the direct reaction of copper and silver salts with elemental selenium in the presence of $NaBH_4$,[4] transforming Ag_2Se or $Cu_{2-x}Se$ NPs into ternary selenides under suitable conditions,[5,8] or thermolysis of suitable metal precursors at high temperature,[9,10] the difficulty in controlling the stoichiometry of the constituent elements often hinders the reproducibility in their synthesis.

Recently, dialkyl dichalcogenides (R_2E_2, where R = alkyl or aryl and E = S, Se, or Te) have been used as low-temperature chalcogen sources for the solution-phase synthesis of metal chalcogenide nanocrystals.[11,12] Not only do these ligands possess relatively weak E−E bonds that can be readily cleaved under mild thermolytic or photolytic conditions, but also their reactivity can be altered by varying organic substituents R on them. The above syntheses under mild conditions have enabled the isolation of metastable nanocrystalline phases with unusual composition and morphology. It has been reported that neat

Received: March 12, 2020

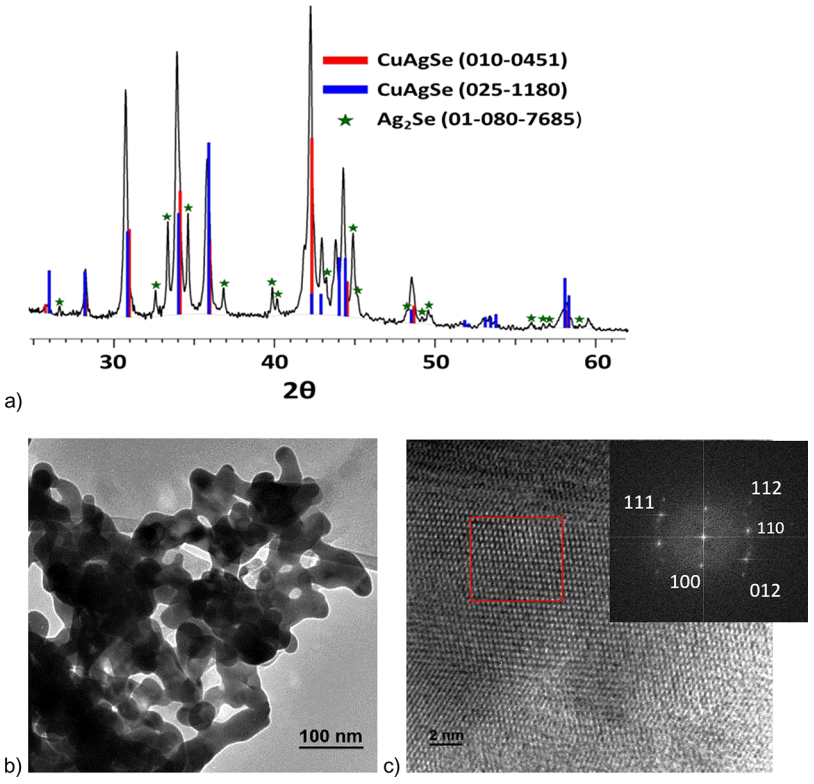

Figure 1. Characterization of AgCuSe NPs obtained at RT from the reaction of Ag(TFA), $Cu(TFA)_2$, and $^tBu_2Se$: (a) XRD pattern; (b) TEM; (c) HRTEM, with FFT analysis given in the inset.

dialkyl dichalcogenides could be thermally or photolytically decomposed to give elemental chalcogen, dialkylchalcogenide (R_2E), and/or organic byproducts via radical scission of the E−E and E−R bonds.[13−15] These observations indicate that the dialkylchalcogenides R_2E can be an interesting alternative chalcogen source for the synthesis of metal chalcogenide nanocrystals under milder conditions because, in addition to all of the advantages that R_2E_2 possess (such as solubility, commercial availability, property optimization by varying R, etc.), the dialkyl chalcogenides R_2E have an additional advantage in that it bypasses the cleavage step of E−E in R_2E_2.

Solution routes to metal chalcogenide nanoparticles (NPs) are vastly appealing not only because they are less energy-intensive than vacuum techniques and have the potential for scalability but also because of the fact that one can exploit the advantage of dialkyl chalcogenides as low-temperature chalcogen sources in the solution phase and, therefore, may synthesize interesting metastable phases of metal chalcogenides.[11,12] Indeed, the silylated chalcogenoethers $(Me_3Si)_2E$ (E = S, Se, Te) have been used in the solution-phase synthesis of metal chalcogenide nanomaterials,[16] although the utilization of relatively less reactive nonsilylated dialkyl chalcogenoethers R_2E has been restricted to the elaboration of thin films in a chemical vapor deposition technique that requires high temperature.[17−22] The use of nonsilylated R_2E ligands, which have high coordinating ability compared to R_2E_2,[23−26] may potentially lead to the isolation of intermediate molecular species, which could throw light on the possible mechanism of molecule-to-NP transformation.[27,28] Starting with well-defined precursors may also overcome the problem of controlling the stoichiometry of the constituent elements, which often hinders the reproducibility in the synthesis of ternary metal chalcogenides. In this work, we sought to explore the divergent reactivity of R_2E (E = Se, S: R = Me, ^{t}Bu) with $Cu(TFA)_2$ and Ag(TFA) (TFA = trifluoroacetate) as a means to establish a well-defined chemical route for the mild synthesis of ternary copper−silver chalcogenide NPs by attempting to isolate and characterize molecular intermediates on the way to materials in the solution phase.

RESULTS AND DISCUSSION

a. Divergent Reactivity of R_2E (R = ^{t}Bu, Me; E = Se, S) with Coinage Metal Reagents: Formation of Ternary Metal Chalcogenide NPs via a Reactive Silver−Copper Molecular Intermediate versus Stable Molecular Complexes. The direct reaction of $^tBu_2Se$ with Ag(TFA) and $Cu(TFA)_2$ at RT resulted in a gradual change in the color of the solution from blue to brown and finally precipitation of a black powder (Figure S1). Warming the reaction mixture at 80 °C increased the yield. The powder X-ray diffraction (XRD) pattern of this black precipitate matched well with those of the previously published XRD results showing a mixture of two phases of ternary silver−copper selenide, AgCuSe, i.e., PDF 010-0451 and 025-1180.[3−5] It also showed a small amount of Ag_2Se NPs [PDF 01-080-7685; ∼5% as quantified using the reference intensity ratio method (Figure 1a]. The scanning electron microscopy (SEM) and transmission electron microscopy (TEM) images show nanometric but somewhat irregular CuAgSe particles (Figures 1b and S2 and S3a), which is not surprising given that synthesis was achieved in the absence of any capping ligand. The high-resolution TEM (HRTEM) images clearly show an interplanar crystal lattice (Figures 1c and S3b). The fast Fourier transform (FFT) image shows the diffraction spots from the (1 0 0), (1 1 0), (1 1 1), (0 1 2), and (1 1 2) crystal planes (Figure 1c, inset). The absence of other elements apart from carbon, copper, silver, and selenium in the

https://dx.doi.org/10.1021/acs.inorgchem.0c00758
Inorg. Chem. XXXX, XXX, XXX−XXX

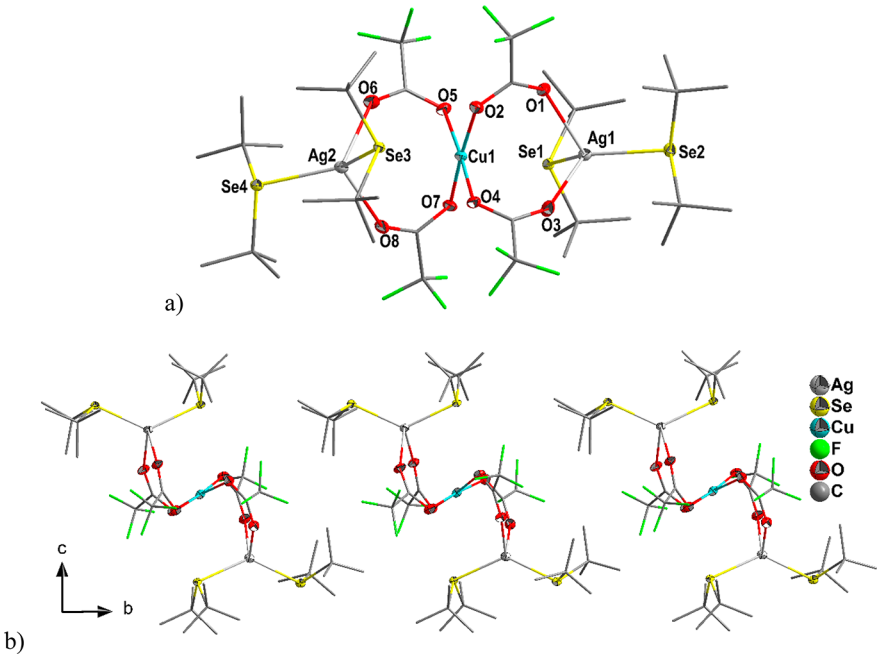

Figure 2. (a) Perspective view of the molecular structure of **1** with 50% probability ellipsoids (hydrogen atoms omitted for clarity). Selected bond lengths (Å) and angles (deg): Ag2−O6 2.436(6), Ag2−O8 2.412(6), Cu1−O2 1.933(6), Cu1−O4 1.944(6), Ag1−Se2 2.581(1), Ag2−Se4 2.601(1); O1−Ag1−O3 93.7(2), Se1−Ag1−O1 102.1(2), Se2−Ag1−O1 109.9(1), Se1−Ag1−Se2 130.1(3), O2−Cu1−O5 87.4(3), O5−Cu1−O7 93.5(3). (b) Extended structure of **1** showing the discrete nature of Ag_2Cu trinuclear units (the shortest intermolecular Ag···Ag interaction being 8.5 Å).

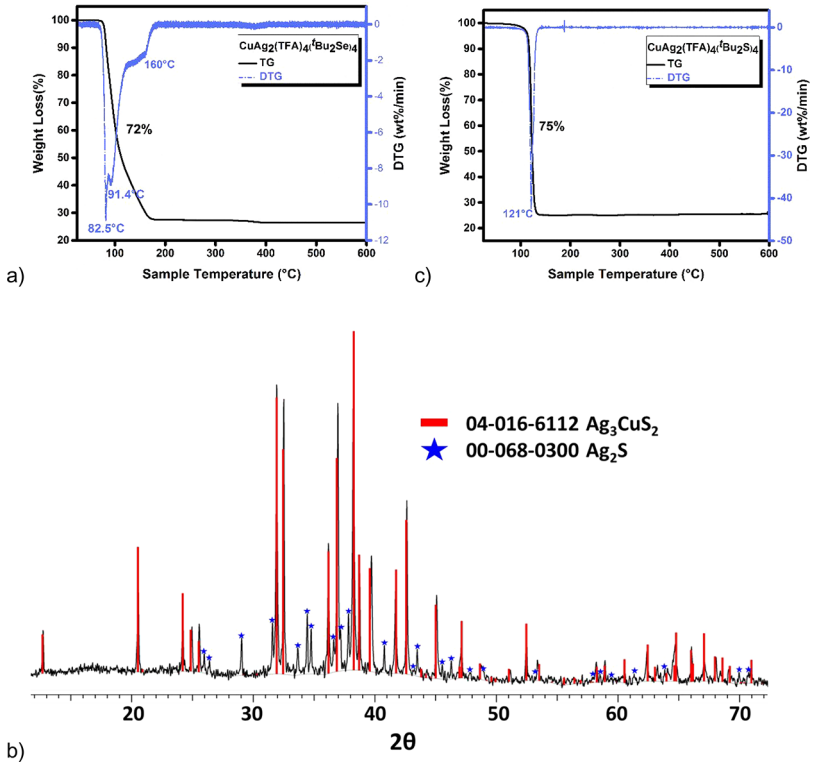

Figure 3. TG−DTG curves of **1** (a), XRD pattern of the powder obtained after decomposition of **2** in refluxing toluene (b), and TG−DTG curves of **2** (c).

energy-dispersive X-ray (EDX) analysis indicates the high purity of the NPs (Figure S4). The EDX analysis of several randomly selected area gives a slightly silver-rich stoichiometry due to the presence of an additional Ag_2Se phase, as indicated by XRD. The NPs were further studied by X-ray photoelectron spectroscopy (XPS) analysis, which shows that the NPs are mainly composed of Cu^+, Ag^+, and Se^{2-} with very small amounts of Cu^{2+} and Se^{4+}, most probably because of the surface oxidation of NPs (Figure S5).[29] The Cu $2p_{3/2}$ state shows the presence of two electronic states located at 932.4 and 934 eV.[27] Because the difference in the binding energies of Cu^0 and Cu^+ is very small (only few millielectronvolts), Auger analysis was carried out by using the

https://dx.doi.org/10.1021/acs.inorgchem.0c00758
Inorg. Chem. XXXX, XXX, XXX−XXX

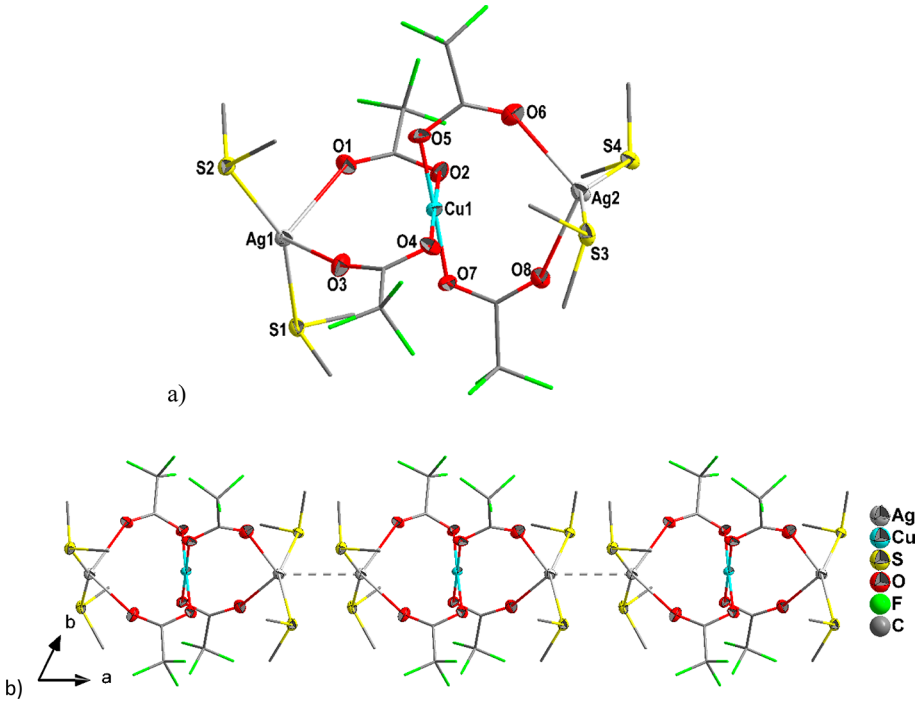

Figure 4. (a) Perspective view of the molecular structure of **4** with 50% probability ellipsoids (hydrogen atoms omitted for clarity). (b) Extended structure with a short Ag···Ag interaction (3.23 Å) among Ag_2Cu trinuclear units to afford a 1D chain. Selected bond lengths (Å) and angles (deg): Ag1−S1 2.458(2), Ag1−S2 2.476(2), Ag1−O1 2.511(6), Ag1−O3 2.528(6), Ag2−S4 2.486(2), Ag2−S3 2.461(2), Ag2−O8 2.501(7), Ag2−O6 2.438(7), Cu1−O2 1.933(5), Cu1−O4 1.946(5), Cu1−O7 1.932(6), Cu1−O5 1.934(6); S1−Ag1−S2 153.63(7), S1−Ag1−O1 107.61(18), S1−Ag1−O3 97.38(16), S2−Ag1−O1 92.93(17), S2−Ag1−O3 94.14(15), O1−Ag1−O3 102.1(2), S4−Ag2−O8 92.99(15), S3−Ag2−S4 148.58(7), S3−Ag2−O8 95.82(15), O6−Ag2−S4 95.93(19), O6−Ag2−S3 108.6(2), O6−Ag2−O8 111.6(3), O2−Cu1−O4 179.2(2), O2−Cu1−O5 88.7(2), O7−Cu1−O2 92.1(2), O7−Cu1−O4 87.9(2), O7−Cu1−O5 178.6(2), O5−Cu1−O4 91.3(2).

Auger parameter.[30] In this case, the Auger parameter is approximately 1850, attributable to Cu^+ for the first chemical state at 932.4 eV. The state located at 934 eV corresponds to Cu^{2+}, as further indicated by the presence of satellite states around 943 eV. The spin−orbit states for Ag $3d_{5/2}$ and $3d_{3/2}$, which appear at 368 and 374 eV, respectively, correspond to Ag^+.[28] The Se $3d_{5/2}$ state from Se^{2-} appears at 53.6 eV.[27,28] The state visible at 58.5 eV can be attributed to Se^{4+}.

Identification of reactive intermediate species operating at the interface of stable molecular complexes and NPs is an important aspect and a key factor to (i) comprehend the mechanism of molecule-to-NP formation and (ii) achieve fine control over their chemical composition and reactivity to optimize the synthetic conditions and properties of the NPs.[27,28] Therefore, attempts were made to identify the species present in the solution before the precipitation of AgCuSe NPs. We succeeded in isolating and characterizing an intermediate molecular species, $[Ag_2Cu(TFA)_4(^tBu_2Se)_4]$ (**1**), in good yield from the reaction mixture. Although **1** is highly reactive and turns black in a few days even at low temperature and in an inert atmosphere, apparently because of the formation of metal selenide NPs, it is stable for a sufficient duration to be characterized by single-crystal XRD, Fourier transform infrared (FT-IR), thermogravimetry−differential thermal gravimetry (TG−DTG), and thermochromic studies. The molecular structure of **1** is based on a spirocyclic metal−oxygen framework. It crystallizes in the orthorhombic space group *Pbca*, and its structure can be conceptually seen as a bidentate interaction of the two monoanionic $\{Ag(\mu\text{-}TFA)_2(^tBu_2Se)_2\}^-$ moieties with an electrophilic Cu^{2+} center (Figure 2a). The two six-membered boat-shaped "AgO_4Cu" rings are fused at a common Cu^{2+} center. The tendency of TFA to act as an assembling ligand to afford heterometallics has previously been highlighted.[31] Two terminal $^tBu_2Se$ ligands present on each of the silver atoms then complete a distorted tetrahedral O_2Se_2 environment around metal centers [if short $Ag^I\cdots Cu^{II}$ interactions (3.589−3.679 Å) are not taken into account], as revealed in the range of angles around the silver center (93.72−131.21°). The Ag−O [2.412(6)−2.436(6) Å] and Ag−Se [2.581(1)−2.601(1) Å] bond lengths compare well with the literature values on the bridging TFA and terminally bonded selenium-containing ligands, respectively.[27,28] The four oxygen atoms around Cu1 are essentially in the same plane and at almost the same distance from the copper [Cu−O = 1.941(6)−1.944(6) Å].[32] These trinuclear Ag_2Cu species are discrete in nature, with the shortest intermolecular Ag···Ag interaction being 8.5 Å (Figure 2b).

The TG studies of **1** confirmed its low thermal stability and high reactivity. The TG curve, recorded under a nitrogen atmosphere, indicates a two-step decomposition in the temperature range 60−160 °C (Figure 3a), with two DTG peaks at 82.5 and 91.4 °C. A residual mass of 28% at 200 °C is consistent with the formation of 1 equiv of AgCuSe + 0.5 equiv of Ag_2Se (calculated value 26.5%) as the end product. The high reactivity of **1** is further evident from the fact that it is transformed to a mixture of AgCuSe and Ag_2Se upon being left in open air for a few hours (Figure S6). It reacts differently with water and gives mainly Ag_2Se, Cu_2Se, and metallic silver (Figure S7 and S8).

A similar reaction with $^tBu_2S$ in toluene did not lead to either a change in color or any precipitation even after stirring for several hours at RT but yielded a black precipitate immediately upon reflux. XRD of this precipitate showed ternary silver−copper sulfide Ag_3CuS_2 (PDF 04-016-6112) as the major phase, along

https://dx.doi.org/10.1021/acs.inorgchem.0c00758
Inorg. Chem. XXXX, XXX, XXX−XXX

with a small amount of Ag_2S (PDF 00-068-0300; Figure S9). Blue crystals of the composition $[Ag_2Cu(TFA)_4(^tBu_2S)_4]$ (**2**) were readily obtained in good yield from the reaction mixture of Ag(TFA), $Cu(TFA)_2$, and $^tBu_2S$ at RT. In the FT-IR spectrum of **2**, the presence of only one strong band at 1715 cm^{-1} due to $\nu_{as}(CO_2)$ (Figure S10)[33,34] suggests a structure similar to that of **1**, where TFA ligands show only one bonding mode. The structure of **2** is indeed similar to that of **1** and is given in Figure S11. Unlike **1**, which gradually turns black even when kept in the dark at low temperature and under an inert atmosphere, complex **2** is stable at RT for several weeks. However, it decomposes in refluxing toluene to give a mixture of Ag_3CuS_2 (PDF 04-016-6112) and Ag_2S (PDF 00-068-0300), with the former being the major phase (Figure 3b). This thermal instability can be explained by the TG studies of **2**, which indicate a single-step decomposition with only one DTG peak at 121 °C (Figure 3c). The presence of a small amount of binary silver chalcogenide Ag_2Se/Ag_2S in the ternary AgCuSe/Ag_3CuS_2 is not always a drawback and may actually be beneficial for certain applications. For example, we have recently shown that the presence of two phases of ternary metal chalcogenide in AgCuSe/TiO_2 composites enhances their photocatalytic activity because of a synergic effect between the two phases.[5]

We then attempted to mimic the above reaction with the Me_2E (E = Se, S) ligands, for which there is no possibility of decomposition via the β-hydrogen elimination pathway.[27,28,35,36] As expected, these reactions yielded molecular complexes of similar composition, $[Ag_2Cu(TFA)_4(Me_2E)_4]$ [E = Se (**3**), S (**4**)], which are kinetically as well as thermally stable. The isostructural **3** and **4** essentially have a structure that is similar to their $^tBu_2E$ (E = Se, S) analogues **1** and **2** at the trinuclear level (Figures 4a and S13a). However, unlike the discrete nature of the Ag_2Cu trinuclear units in **1** and **2**, these units have strong enough Ag···Ag interaction (2.5−3.23 Å) in **3** and **4** to give 1D chain (Figures 4b and S13b). As a result, the Ag−O bond lengths are slightly longer here [2.438(7)−2.528(6) Å in **4** vs 2.391(4)−2.436(6) Å in **1** and **2**]. The four oxygen atoms around Cu1 are arranged in the same plane, with the Cu−O distances [1.932(6)−1.946(5) Å] being comparable to those found in **1** and **2**. The Ag−S distances are spread in the range 2.458(2)−2.486(2) Å. The polymeric nature of **3** and **4** is reflected in their TG−DTG curves, which show a multistep thermal decomposition that lasts well beyond 300 °C (Figure S14). Upon decomposition under an inert atmosphere at 350 °C, **3** is transformed to a mixture of AgCuSe and Ag_2Se (and a very small impurity of the metallic silver; Figure S15).

The silylated chalcogenoethers $(Me_3Si)_2E$ (E = S, Se, Te) are important reagents for the solution-phase synthesis of metal chalcogenides under mild conditions.[16] However, their mechanism has been the subject of many speculations. Formation of a sulfide-bridged intermediate, $[(NHC)_2Ag_2(\mu\text{-}S)]$ (NHC = N-heterocyclic carbene), has been suggested during the formation of Ag_2S NPs from the RT reaction of $(Me_3Si)_2S$ with (NHC)AgX (X = halide), although no structural evidence was presented.[37] On the other hand, the reaction of $(Me_3Si)_2E$ with the related (NHC)Cu(OAc) was shown to afford thermally stable complexes $[(NHC)Cu\text{-}ESiMe_3]$ (E = S, Se, Te) at low temperature,[38] suggesting the conversion of chalcogenoethers to chalcogenolates, before affording metal chalcogenide NPs. Using the bulkier nonsilylated dialkylselenide $^tBu_2Se$, which is slightly less reactive than its silylated counterpart but still gives metal selenide NPs with group 11 metal reagents at RT, we have been able to isolate reactive intermediates $[Cu_2(TFA)_2(^tBu_2Se)_3]$ and $[Ag(TFA)(^tBu_2Se)_2]$, which confirmed that $Cu_{2-x}Se$ and Ag_2Se NPs are formed via these intermediates.[27,28] The synthesis of ternary metal chalcogenide materials is even more challenging, and very few single-source precursors (SSPs) are reported so far for them. Not only do the heterometallics $[Ag_2Cu(TFA)_4(R_2E)_4]$ (R = Me, ^{t}Bu; E = S, Se) described here fill this clear void of SSPs for such ternary chalcogenide materials, but, more importantly, some of them were isolated as intermediates with tailored reactivity, which can be used to investigate the fundamentals of the nucleation and growth of these ternary materials.

The high reactivity of $^tBu_2E$ (E = Se, S) to give metal chalcogenide NPs under mild conditions can be attributed to the availability of a decomposition path via β-hydrogen elimination, which first leads to the formation of *tert*-butylchalcogenol and then a chalcogenide ligand (eqs S1−S3).[39] This mechanism finds support from the above-mentioned isolation of chalcogenolate complexes $[(NHC)Cu\text{-}ESiMe_3]$ (E = S, Se, Te) and the proposed sulfide-bridged intermediate $[(NHC)_2Ag_2(\mu\text{-}S)]$ during the reaction of $(Me_3Si)_2S$ with (NHC)Cu(OAc) and (NHC)AgX, respectively.[37,38] A higher reactivity of selenide precursors in comparison to analogous sulfide precursors has previously been demonstrated and explained on the basis of density functional theory (DFT) calculations.[12] The coordinated $^tBu_2E$ (E = Se, S) ligands play a dual role in the formation of metal chalcogenide NPs, i.e., a facile source of chalcogens and a reducing reagent to get the desirable 1+ oxidation state of the copper center.

b. DFT Calculations. DFT calculations were performed on $[Ag_2Cu(TFA)_4(R_2E)_4]$ [R = ^{t}Bu, E = Se (**1**), S (**2**); R = Me, E = Se (**3**), S (**4**)] to gain information about their electronic structures and, consequently, their reactivity and properties. Popular quantum-mechanical descriptors, e.g., the highest occupied molecular orbital (HOMO)−lowest unoccupied molecular orbital (LUMO) energies, play a major role in governing a wide range of chemical interactions. The frontier molecular orbital gives insight into the reactivity of the molecule, and the active site can be demonstrated by the distribution of frontier orbitals. The HOMO−LUMO energy gap generally implies the kinetic energies and chemical reactivity rate. The energy gap between the HOMO and LUMO electronic levels is a critical parameter that corresponds to the energy difference between the ionization potential and electron affinity of a molecular species or material and determines its electronic, optical, redox, and transport (electrical) properties. The band gap is also referred to as the transport gap because it represents the minimum energy necessary to create a positive charge carrier somewhere in the material minus the energy gained by adding a negative charge carrier. The HOMO and LUMO energies as well as the HOMO−LUMO energy gaps of **1**−**4** are presented in Table 1. The HOMO−LUMO gaps of 0.25, 3.13, 2.09, and 3.06 eV are calculated for **1**−**4**, respectively, which confirm the

Table 1. HOMO and LUMO Energies and the HOMO−LUMO Band Gap for 1−4

molecular species	HOMO	LUMO	ΔE
$Ag_2Cu(TFA)_4(^tBu_2Se)_4$ (**1**)	−3.68176	−3.43226	0.25
$Ag_2Cu(TFA)_4(^tBu_2S)_4$ (**2**)	−0.15735	2.9695	3.13
$Ag_2Cu(TFA)_4(Me_2Se)_4$ (**3**)	−0.43356	1.659036	2.09
$Ag_2Cu(TFA)_4(Me_2S)_4$ (**4**)	−0.63741	2.42129	3.06

https://dx.doi.org/10.1021/acs.inorgchem.0c00758
Inorg. Chem. XXXX, XXX, XXX−XXX

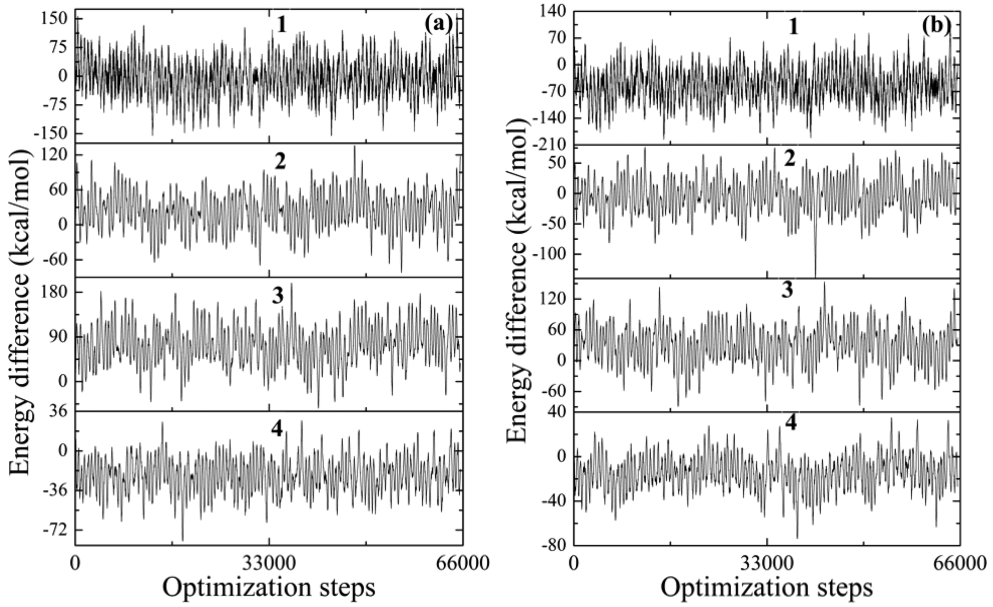

Figure 5. Fluctuation in energy of the system as a function of the optimization steps for **1**−**4** at 353 (a) and 393 K (b) (molecular dynamics simulations).

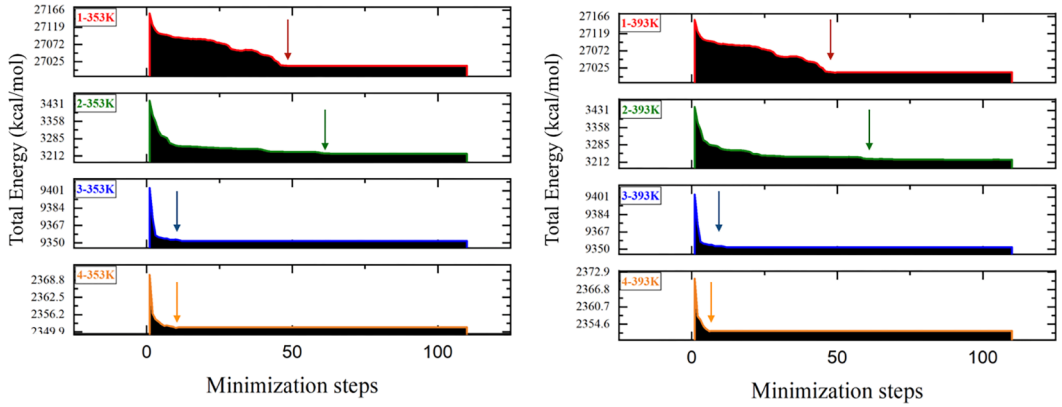

Figure 6. Steps of optimized structures as a function of the total energy for **1**−**4** at 353 and 393 K.

kinetic instability and higher chemical reactivity of **1**. This is further confirmed by the temperature-dependent simulation of **1**−**4** at 353 and 393 K, performed for 200 ps with a time step of 1 fs (Video S1). Figure S16 gives some intrinsic insight into the structural properties and stabilities of **1**−**4** simulated under constant pressure and varying temperatures. Compared to **2**−**4**, the reactive intermediate **1** shows the highest fluctuation in the total energy difference ΔE variation and takes the highest steps to reach the equilibrium (Figures 5 and 6). The Langevin thermostat and production with a Nose−Hoover (NVT) ensemble for 200 ps for **1**−**4**, where the number of atoms (N), volume (V), and temperature (T) were kept constant, represent the stability of the structures as a function of the total energy (Figure 7). The high total energy variation can only be observed for **1** at both 353 and 393 K, which is in accordance with its structural deformation, as depicted previously in Figure S16. The isothermal and isobaric (NPT) ensemble for 200 ps as a function of the total energy for **1**−**4** at 353 and 393 K temperature, where the number of atoms (N), pressure (P), and temperature (T) were conserved, is depicted in Figure S17. The observed large volumetric expansion for **1** at 353 K and less expansion of volume at 393 K indicates its instability at 353 K compared to **2**−**4**. Figure S18 shows the pair distribution function $g(r)$, which accounts for the number of neighbors for each atom that are within a given cutoff range (in our case, at r = 3.5) around its position by analysis of the structural stability at different temperatures. $g(r)$ measures the probability of finding a particle at distance r given that there is a particle at position 0; it is essentially a histogram of interparticle distances. The pair distribution function is normalized by the number density of the particles (i.e., total number of particles divided by the simulation cell volume).

c. Thermochromic Behavior of 1. Interestingly, when taken in a coordinating solvent (or even in contact with the vapor of this solvent), the color of **1** changes from blue (273 K and below) to green at RT (Figures 8, inset, and S19 and Video S2). Figure 8 shows the evolution of the peaks at 463 nm (blue) and 543 nm (green) in the absorption spectrum of **1** in tetrahydrofuran (THF) in terms of a blue-to-green (B/G) ratio as a function of the temperature. As the temperature increases, the B/G ratio continuously decreases until the complex decomposes at about 330 K. The simulated UV−visible absorption spectra of **1**−**4** at RT are presented in Figure S20. While **1** has relatively higher intensity of the absorption bands

https://dx.doi.org/10.1021/acs.inorgchem.0c00758
Inorg. Chem. XXXX, XXX, XXX−XXX

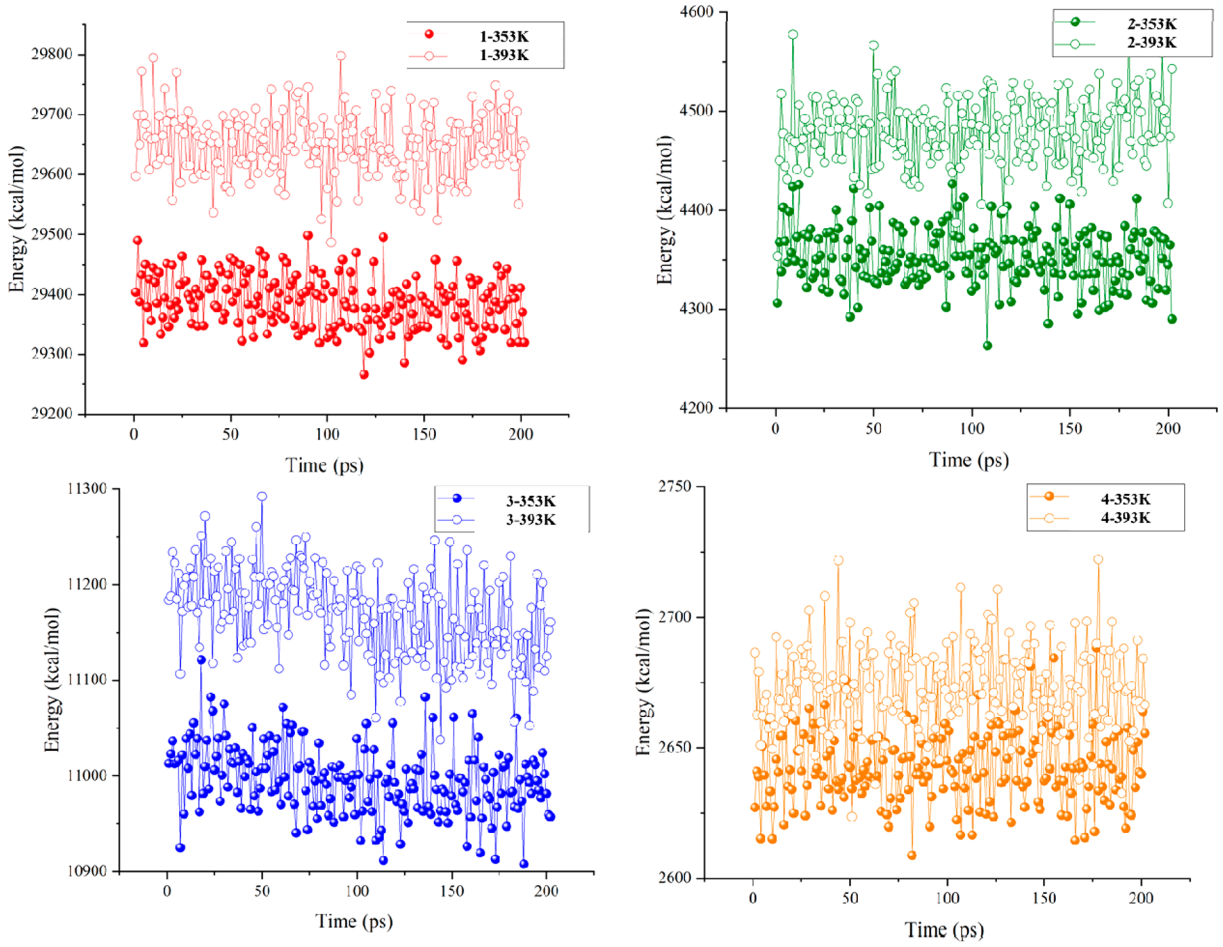

Figure 7. Langevin thermostat and production with the Nose−Hoover (NVT) ensemble for 200 ps as a function of the total energy for **1**−**4** at 353 and 393 K.

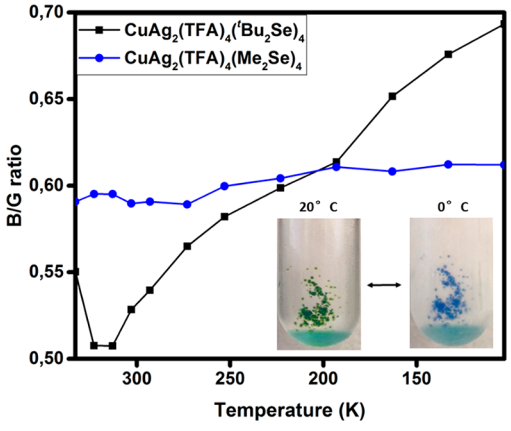

Figure 8. Change in the absorption intensity of the blue (463 nm) and green (543 nm) peaks of **1** and **3** taken in THF, in terms of the B/G ratio, as a function of the temperature. The photographs at the bottom show two different colors of **1** at two different temperatures.

and shows the most dominating peak at around 550 nm, compounds **2**−**4** have the most dominant absorption bands in the region 430−460 nm. As expected, the absorption spectrum of the kinetically and thermally instable **1** shows significant changes at 353 K (Figure 9a), whereas **4**, which is thermally stable, presents similar absorption peaks at high temperature (although of slightly different intensity; Figure 9b).

Because **1** is not thermochromic in a noncoordinating solvent such as toluene (Figure S21), it is very probable that the above reversible phenomenon is due to coordination/discoordination of the THF molecule with the copper atom. In the X-ray structure of **1** at 100 K, the copper center has weak intramolecular interactions with silver (3.59−3.68 Å) and selenium atoms (3.87−3.95 Å). At RT, these interactions are expected to further weaken, thus allowing solvent THF molecules to get weakly coordinated with the copper center, which would, by virtue of a dynamic pseudo-Jahn−Teller effect, cause a red shift in the absorption (blue to green).[40−42] This theory is further supported by the fact that complex **2**, which has stronger Cu···S interaction (3.55 Å), or **3** and **4**, which are structurally more rigid because of additional intermolecular Ag··· Ag interaction (2.5−3.23 Å) among the Ag_2Cu trinuclear units, do not demonstrate any visible thermochromism and the B/G ratio does not change significantly with the temperature (Figure 8 and Video S3). Unfortunately, our efforts to corroborate further the above theory by measuring the single-crystal X-ray structure of **1** at RT were not successful because of the instability of this compound, which decomposed after a few frames of data collection.

CONCLUSIONS

Mild syntheses of ternary coinage metal chalcogenides AgCuSe and Ag_3CuS_2 from the reaction of Ag(TFA) and $Cu(TFA)_2$ with $^tBu_2Se$ or $^tBu_2S$ are presented. The successful isolation and

https://dx.doi.org/10.1021/acs.inorgchem.0c00758
Inorg. Chem. XXXX, XXX, XXX−XXX

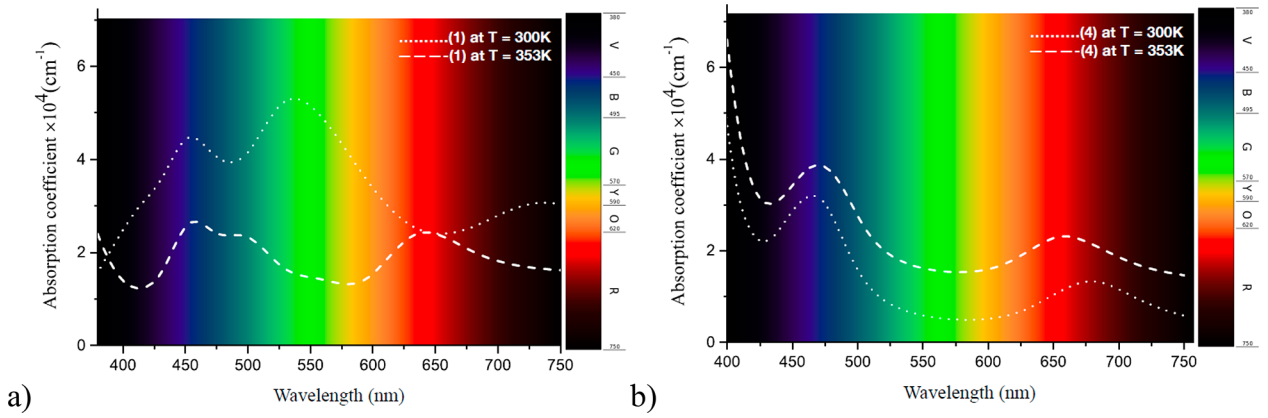

Figure 9. Simulated UV−visible absorption spectra of **1** (a) and **4** (b) at variable temperature.

characterization of intermediate species during the course of these reactions, $[Ag_2Cu(TFA)_4(^tBu_2E)_4]$ [E = Se (**1**), S (**2**)], establishes a precursor-mediated pathway for the formation of ternary metal chalcogenides. The highly reactive intermediate **1** is thermally and kinetically instable, as confirmed by TG studies and DFT calculations, and shows an interesting thermochromic behavior (green at 20 °C and blue at 0 °C). In contrast, the analogue complexes with $^tBu_2S$ and Me_2E ligands, i.e., $[Ag_2Cu(TFA)_4(R_2E)_4]$ [R = ^{t}Bu, E = S (**2**); R = Me, E = Se (**3**), S (**4**)], are kinetically stable and nonthermochromic in nature. In addition to the utility of these heterometallic precursors in the solution-phase synthesis of ternary metal chalcogenide NPs, their tailored reactivity can also be used to study the fundamentals of nucleation and growth of ternary materials.

EXPERIMENTAL SECTION

General Procedures. We performed all of the manipulations under an argon atmosphere using standard Schlenk and glovebox techniques. Solvents were dried using MB SPS-800 and used without further purification. Silver trifluoroacetate (Aldrich), di-*tert*-butyl selenide (SAFC Hitech), di-*tert*-butyl sulfide and dimethyl sulfide (TCI Europe NV), and dimethyl selenide and copper(II) trifluoroacetate hydrate (Alfa Aesar) were purchased and used without further purification. A copper(II) trifluoroacetate/tetrahydrofuran adduct was synthesized in the laboratory from the reaction of Cu_2O and TFAH in toluene and then extracted from THF. The IR spectra were obtained as Nujol mulls on a Bruker Vector 22 FT-IR spectrometer at RT and registered from 4000 to 400 cm^{-1}. Scanning electron microscopy (SEM) measurements were performed on a Hitachi S800 system. Transmission electron microcsopy (TEM) experiments were performed using a JEM-2100F system with 200 kV field emission (FE) and a JEOL 2010 LaB_6 system with 200 kV FE. We used a Bruker D8 Advance A25 system with Cu $K\alpha_1$ + 2 (λ = 0.154184 nm) radiation at 50 kV and 35 mA to measure the X-ray diffraction (XRD) patterns of the NPs. The copper, silver, sulfur, and selenium contents were determined by inductively coupled plasma optical emission spectroscopy (ICP-OES). Thermogravimetric analyses (TGA) were performed with a TGA/differential scanning calorimetry 1 STARe system from Mettler Toledo. Around 8 mg of the sample was sealed in a 100 μL aluminum crucible in the glovebox and heated under an argon atmosphere at a heating rate of 5 °C/min. Diffusion-reflectance measurements were performed on a homemade apparatus. The sample was illuminated by an eq 99X laser-driven point source of the lamp, and it was reimaged on the sample by two 100-m-focal-length, 2-in.-diameter MgF_2 lenses. The emitted light from the sample was collected by an optical fiber connected to a Jobin-Yvon TRIAX320 monochromator equipped with a cooled charge-coupled detector (CCD). The resolution of the detection system was 2 nm. For temperature variation, the sample was placed on a cooling stage from LINKAM Ltd. DSC600, which allowed one to vary the temperature using liquid nitrogen.

Synthesis of CuAgSe NPs and Isolation of a Silver−Copper Heterometallic Molecular Intermediate. A reaction mixture of $Cu(TFA)_2(THF)$ (0.05 g, 0.14 mmol), Ag(TFA) (0.03 g, 0.14 mmol), and $^tBu_2Se$ (0.1 mL, 0.56 mmol) was stirred in the absence of any solvent at RT, which led to a gradual change in the color of the solution from blue to brown, and finally a black powder was precipitated. After the reaction mixture was stirred for 1.5 h, the black precipitate was isolated, washed with ethanol several times, and dried at RT. The powder XRD of this black precipitate confirmed it to be CuAgSe NPs containing also ∼5% of Ag_2Se NPs.

We then made attempts to isolate intermediate molecular species present in the solution during the course of the above reaction. We carried out the above reaction under varied conditions (different reaction times and solvents such as toluene, THF, diethyl ether, etc.) in order to avoid black precipitation and to isolate molecular species. In one such optimized reaction, 0.20 mL of $^tBu_2Se$ (1.10 mmol) was added to a blue toluene solution (20 mL) containing $Cu(TFA)_2(THF)$ (0.1 g, 0.28 mmol) and Ag(TFA) (0.06 g, 0.28 mmol), and the resulting solution was stirred for 15 min at RT. After that, the solution was concentrated under vacuum and layered with *n*-pentane (10 mL) to obtain dark-blue crystals of $[Ag_2Cu(TFA)_4(^tBu_2Se)_4]$ (**1**) along with a few colorless crystals of the composition $[Cu_2(TFA)_2(^tBu_2Se)_3]$ (**a**). The mother liquor was separated through a cannula and concentrated to give more of compound **a**. The formation of compound **a**, which was previously reported by us,[27] can be explained by the fact that only half of $Cu(TFA)_2$ is consumed during formation of the heterometallic **1**, which has a 2:1 ratio of the silver and copper atoms. The blue crystals of **1** were isolated and washed with cold *n*-pentane. Yield: 0.17 g (52%). FT-IR (Nujol, cm^{-1}): 1712s, 1460s,1381s, 1200m, 1139m, 729m, 842w, 793w, 525w.

Alternatively, compound **1** can also be synthesized in a better yield and without having any contamination of the copper species (**a**) by reacting $[Ag_2Cu(TFA)_4(Me_2Se)_4]$ (**3**) (see the synthetic details of **3** below) with $^tBu_2Se$ in toluene. In this reaction, $^tBu_2Se$ (0.07 mL, 0.37 mmol) was dropwise added to a solution of **3** (0.11 g, 0.09 mmol) in toluene (3 mL), which led to a change in the color of the solution from blue to green (Figure S22). This mixture was stirred at RT for 20 min and then layered with *n*-pentane (7 mL). Upon diffusion, blue solution was given, from which blue crystals of **1** were obtained at 0 °C. The mother liquor was removed through a cannula, and the crystals were washed with cold *n*-pentane. Yield: 0.08 g (71%). **1** is highly reactive and unstable and turns black in 1−2 days even when kept at low temperature and under an inert atmosphere. This precluded us to perform its elemental analysis. FT-IR (Nujol, cm^{-1}): 1714s, 1463s,1382s, 1205m, 1144m, 733m, 845w, 798w, 526w.

Synthesis of Ag_3CuS_2 NPs and Isolation of a Silver−Copper Heterometallic Molecular Intermediate. In contrast to the above reaction, the reaction of $Cu(TFA)_2(H_2O)$ (0.3 g, 0.96 mmol), Ag(TFA) (0.21 g, 0.96 mmol), and $^tBu_2S$ (0.85 mL, 4.80 mmol) in

https://dx.doi.org/10.1021/acs.inorgchem.0c00758
Inorg. Chem. XXXX, XXX, XXX−XXX

Table 2. Crystallographic and Refinement Data for 1−4

	1	2	3	4
empirical formula	$C_{40}H_{72}Ag_2CuF_{12}O_8Se_4$	$C_{40}H_{72}Ag_2CuF_{12}O_8S_4$	$C_{48}H_{72}Ag_6Cu_3F_{36}O_{24}Se_{12}$	$C_{16}H_{24}Ag_2CuF_{12}O_8S_4$
fw	1504.1	1316.5	3502.4	979.9
cryst syst	orthorhombic	monoclinic	monoclinic	triclinic
space group	*Pbca*	*C*2/*c*	$P2_1/n$	$P\bar{1}$
a (Å)	17.9685(15)	17.4632(11)	17.0247(11)	10.4336(10)
b (Å)	22.642(4)	16.5079(9)	31.466(3)	11.0465(9)
c (Å)	27.703(3)	20.0811(14)	19.6823(19)	16.3292(10)
α (deg)	90	90	90	75.224(6)
β (deg)	90	101.451(7)	104.751(8)	86.689(6)
γ (deg)	90	90	90	64.143(9)
V (Å^3)	11270(2)	5673.8(6)	10196.4(15)	1634.5(3)
Z	8	4	4	2
μ (mm^{-1})	3.73	1.28	6.15	2.19
temp (K)	100	150	150	150
measd reflns	48269	38823	79599	14879
indep/obsd [$I > 2\sigma(I)$] reflns	13493/7579	7289/5967	24441/13442	14879/9923
R_{int}	0.086	0.041	0.096	0.09
restrains/param	69/656	533/428	1080/1150	0/396
GOF	1.03	1.10	1.61	1.07
R [$F^2 > 2\sigma(F^2)$]	0.069	0.046	0.180	0.071
wR (F^2)	0.204	0.119	0.507	0.224
residual electron density (e/Å)	−1.67 to 2.55	−1.07 to 0.68	−3.24 to 13.92	−1.53 to 3.47
CCDC	1903337	1968807	1903338	1968808

toluene (30 mL) did not lead to any change in color at RT. However, under reflux, the color of the solution changed from dark blue to dark green, and after some time, black powder was precipitated. After 3 h of reflux, the precipitates were collected and washed thoroughly with ethanol and then dried at RT. The final product, when characterized by a powder XRD technique, was found to be a mixture of Ag_3CuS_2 (70%) and Ag_2S (30%). Yield: 0.09 g (42% by weight Ag).

Because the reaction medium was stable at RT, an attempt to isolate intermediate molecular species present in the solution during the course of the above reaction was relatively straightforward. The green toluene solution (30 mL) containing $Cu(TFA)_2(H_2O)$ (0.32 g, 1 mmol), Ag(TFA) (0.22 g, 1 mmol), and $^tBu_2S$ (0.7 mL, 4 mmol), after stirring for 1 h, was concentrated and layered with *n*-hexane to obtain dark-blue crystals of $[Ag_2Cu(TFA)_4(^tBu_2S)_4]$ (**2**) along with a few green crystals later identified as $[Cu(TFA)_2(^tBu_2S)]$ (**b**) by elemental analysis. The formation of compound **b** can be explained by the fact that only half of $Cu(TFA)_2$ is consumed during formation of the heterometallic **2**, which has a 2:1 ratio of the silver and copper atoms. The blue crystals of **2** were isolated and washed with cold *n*-pentane. Yield: 0.58 g (62%). FT-IR (Nujol, cm^{-1}): 1694s, 1465s, 1367s, 1200s, 842m, 790m, 724m, 668w, 615w, 592w, 522w. The reaction in the right stoichiometry [$Cu(TFA)_2(H_2O)$ (0.2 g, 0.64 mmol), Ag(TFA) (0.28 g, 1.29 mmol), and $^tBu_2S$ (0.46 mL, 2.58 mol)] improved the yield of the product (78%) and avoided contamination of the copper species (**b**). Calcd for $C_{40}H_{72}Ag_2CuF_{12}O_8S_4$ (1316.5): C, 36.46; H, 5.47; Ag, 16.38; Cu, 4.83; S, 9.74. Found: C, 36.21; H, 5.29; Ag, 16.23; Cu, 4.73; S, 9.65. FT-IR (Nujol, cm^{-1}): 1694s, 1465s, 1367s, 1200s, 842m, 790m, 724m, 668w, 615w, 592w, 522w. Unlike **1**, **2** is stable for several days when kept at low temperature/RT and under an inert atmosphere.

Synthesis of Stable $[Ag_2Cu(TFA)_4(Me_2Se)_4]$ (E = Se, S). *$[Ag_2Cu(TFA)_4(Me_2Se)_4]$ (**3**).* After the dropwise addition of Me_2Se (0.1 mL, 1.30 mmol) to a blue solution of $Cu(TFA)_2(THF)$ (0.1 g, 0.28 mmol) and Ag(TFA) (0.12 g, 0.54 mmol) in THF (20 mL), the resulting solution was stirred for 2 h at RT. After the solution was concentrated, it was layered with *n*-hexane (10 mL) to obtain dark-blue crystals of **3**. The mother liquor was removed through a cannula, and the crystals were isolated and washed with cold *n*-pentane. Yield: 0.19 g (56%). Calcd for $C_{16}H_{24}Ag_2CuF_{12}O_8Se_4$ (1167.5): C, 16.44; H, 2.06; Ag, 18.48; Cu, 5.44; Se, 27.06. Found: C, 16.40; H, 1.98; Ag, 18.45; Cu, 5.40; Se, 26.90. FT-IR (Nujol, cm^{-1}): 1715s, 1456s, 1377s, 725s, 970m, 928m, 846m, 793m, 521m, 601w, 427w.

Using the above method, compound $[Ag_2Cu(TFA)_4(Me_2S)_4]$ (**4**) was synthesized from $Cu(TFA)_2(H_2O)$ (0.10 g, 0.32 mmol), Ag(TFA) (0.14 g, 0.64 mmol), and Me_2S (0.1 mL, 1.47 mmol) in Et_2O (30 mL) and crystallized as dark-blue crystals by layering the concentrated solution with *n*-hexane. Yield: 0.22 g (68%). Calcd for $C_{16}H_{24}Ag_2CuF_{12}O_8S_4$ (979.87): C, 19.60; H, 2.45; Ag, 22.02; Cu, 6.48; S, 13.09. Found: C, 19.43; H, 2.34; Ag, 21.79; Cu, 6.43; S, 12.89. FT-IR (Nujol, cm^{-1}): 1682s, 1457s, 1377s, 1198s, 1151s, 726s, 1036m, 987m, 843m, 792m, 679w, 668w, 606w, 523w.

*Decomposition of **1** in Air.* Upon exposure to air, the crystals of **1** (0.05 g) turned black in a few hours. The powder XRD on these black crystals after 3 days showed the presence of CuAgSe and Ag_2Se phases in approximately equal proportions (Figure S6).

*Hydrolysis of **1**.* The reaction of water (0.5 mL) with **1** (0.05 g taken in 5 mL toluene) at an ambient atmosphere resulted in a light-gray solution within the first few minutes, which upon further stirring for 3 h gave black precipitates consisting mainly of Cu_2Se, Ag_2Se, and metallic silver, as revealed by powder XRD (Figures S7 and S8).

*Thermal Decomposition of **2**.* A total of 0.14 g of dark-blue crystals of **2** was dissolved in toluene (30 mL). After the addition of 0.5 mL of $^tBu_2S$, the solution was refluxed for 1 h to obtain black precipitates. Powder XRD results of this sample confirmed the presence of Ag_3CuS_2 as a major phase along with Ag_2S (Figure 3b).

*Thermal Decomposition of **3**.* A total of 0.15 g of **3** was decomposed in the solid state at 350 °C for 2 h in an inert atmosphere to obtain black precipitates, the powder XRD of which showed the presence of CuAgSe as a major phase along with small amounts of Ag_2Se and metallic silver (Figure S15).

X-ray Crystallography. Crystals of **1**−**4** were obtained as described in the synthetic procedure. Crystal structures were determined using molybdenum radiation (λ = 0.71073 Å) on an Oxford Diffraction Gemini diffractometer equipped with an Atlas CCD. Intensities were collected at 100 K by means of *CrysAlisPro* software.[43] Reflection indexing, unit-cell parameter refinement, Lorentz-polarization correction, peak integration, and background determination were carried out with *CrysAlisPro* software.[43] An analytical absorption correction was applied using the modeled faces of the crystal.[44] The resulting sets of *hkl* were used for structure solutions and refinements.

https://dx.doi.org/10.1021/acs.inorgchem.0c00758
Inorg. Chem. XXXX, XXX, XXX−XXX

The structures were solved with the *ShelXT*[45] structure solution program using intrinsic phasing and by using *Olex2*[46] as the graphical interface. The model was refined with version 2018/3 of *ShelXL*[47] using least-squares minimization. Some selected crystallographic and refinement data of **1**−**4** are listed in Table 2.

Computational Details. In the present work, we have performed electronic structure calculations within DFT,[48,49] which is implemented in the Vienna Ab Initio Simulation Package (*VASP*) code.[50] The projector-augmented-wave potentials were adopted to describe the difference between cores and valence electrons.[51] The generalized gradient approximation (GGA) functional in the form of the Perdew, Burke, and Ernzerhof functional was adopted to describe the exchange and correlation potentials.[52] We have chosen *k*-point sampling (5 × 4 × 3), (5 × 5 × 5), (5 × 2 × 5), and (7 × 7 × 5) for **1**−**4**, respectively, for Brillouin zone integration in *k* space. Here, the *k*-point mesh is generated by the Monkhorst−Pack scheme.[53] The kinetic energy cutoff for the plane-wave basis set is 600 eV. Atoms are optimized until the force per atom in the unit cell was converged within 10^{-3} eV/Å. The energy convergence criterion per self-consistent field is 1×10^{-6} eV. For simplistic visualization of the structural configurations at various temperatures, e.g., 353 and 393 K, we have used[54] a classical molecular dynamic with a focus on material modeling. Visual molecular dynamics[55] and OVITO[56] were used to visualize the molecular dynamics trajectories of various structural configurations. The structural minimization was performed using the Polak−Ribiere version of the conjugate gradient algorithm coupled with *NPT*[57] (isothermal and isobaric) and *NVT*[58] (Langevin thermostat and production with Nose−Hoover) ensembles using the universal force field[59] for all of the structural configurations. The simulation was performed for 200 ps with a time step of 1 fs (Video S1). Moreover, we have also analyzed the pair correlation function $g(r)$, which accounts for the number of neighbors for each particle that are within a given cutoff range (in our case at r = 3.2) around its position by analysis of the structural stability at different temperatures.

The electronic properties of materials with different configurations were calculated by employing the GGA functional. The HOMO and LUMO energies of all compounds are presented in Table 1. The electronic absorption relates to the transition from the ground state to the first excited state and is mainly described by one-electron excitation from HOMO to LUMO.[60] The optical absorption coefficient has been extracted from the imaginary part of the complex dielectric function, $\varepsilon(\omega) = \varepsilon_r(\omega) + \varepsilon_i(\omega)$, where $\varepsilon_r(\omega)$ is the real part and $\varepsilon_i(\omega)$ is the imaginary part of the complex dielectric function.[61] The optical absorption coefficient is given as

$$\alpha = \sqrt{2}\,\omega\sqrt{|\varepsilon(\omega)| - \varepsilon_r(\omega)} \quad (1)$$

where $|\varepsilon(\omega)| = \sqrt{\varepsilon_r^2(\omega) + \varepsilon_i^2(\omega)}$ is the relative dielectric constant.

■ ASSOCIATED CONTENT

Supporting Information

The Supporting Information is available free of charge at https://pubs.acs.org/doi/10.1021/acs.inorgchem.0c00758.

Digital images of the synthesis, reactivity, and thermochromic behavior of **1**, SEM, TEM, HRTEM, size distribution curve, EDX, and XPS analysis of AgCuSe NPs, additional XRD patterns of AgCuSe and Ag_3CuS_2, FT-IR of **1**−**4**, X-ray structures of **2** and **3**, TG-DTG curves of **3** and **4**, additional figures related to DFT calculations and simulated UV−visible spectra of **1**−**4**, and decomposition pathway of $^tBu_2Se$ via β-hydrogen elimination (PDF)

Video of the temperature-dependent simulation of **1**−**4** at 353 and 393 K (MP4)

Video of thermochromic behavior of **1** (MOV)

Video of nonthermochromic behavior of **3** (MP4)

Accession Codes

CCDC 1903337−1903338 and 1968807−1968808 contain the supplementary crystallographic data for this paper. These data can be obtained free of charge via www.ccdc.cam.ac.uk/data_request/cif, or by emailing data_request@ccdc.cam.ac.uk, or by contacting The Cambridge Crystallographic Data Centre, 12 Union Road, Cambridge CB2 1EZ, UK; fax: +44 1223 336033.

■ AUTHOR INFORMATION

Corresponding Author

Shashank Mishra − *Institut de Recherches sur la Catalyse et l'Environnement de Lyon (IRCELYON), Université Lyon, Université Claude Bernard Lyon 1, CNRS, UMR 5256, 69626 Villeurbanne, France;* orcid.org/0000-0003-2846-4221; Email: shashank.mishra@ircelyon.univ-lyon1.fr; Fax: (+33) 472445399

Authors

Sweta Gahlot − *Institut de Recherches sur la Catalyse et l'Environnement de Lyon (IRCELYON), Université Lyon, Université Claude Bernard Lyon 1, CNRS, UMR 5256, 69626 Villeurbanne, France*

Erwann Jeanneau − *Centre de Diffractométrie Henri Longchambon, Université Lyon, Université Claude Bernard Lyon 1, 69100 Villeurbanne, France*

Deobrat Singh − *Condensed Matter Theory Group, Department of Physics and Astronomy, Uppsala University, 75120 Uppsala, Sweden*

Pritam Kumar Panda − *Condensed Matter Theory Group, Department of Physics and Astronomy, Uppsala University, 75120 Uppsala, Sweden;* orcid.org/0000-0003-4879-2302

Yogendra Kumar Mishra − *Mads Clausen Institute, NanoSYD, University of Southern Denmark, Alsion 2, Denmark;* orcid.org/0000-0002-8786-9379

Rajeev Ahuja − *Condensed Matter Theory Group, Department of Physics and Astronomy, Uppsala University, 75120 Uppsala, Sweden;* orcid.org/0000-0003-1231-9994

Gilles Ledoux − *Institut Lumière Matière, Université Lyon, Université Claude Bernard Lyon 1, CNRS, 69626 Villeurbanne, France;* orcid.org/0000-0002-0867-1285

Complete contact information is available at: https://pubs.acs.org/10.1021/acs.inorgchem.0c00758

Author Contributions

The manuscript was written through contributions of all authors. All authors have given approval to the final version of the manuscript.

Notes

The authors declare no competing financial interest.

■ ACKNOWLEDGMENTS

S.G. thanks the French ministry of higher education for her Ph.D. grant (doctoral school of chemistry, Lyon). Authors also thank L. Burel (TEM), Y. Aizac (powder XRD), N. Bonnet (ICP elemental analysis), and Dr. L. Cardenas (XPS) of IRCELYON. D.S., P.K.P., and R.A. thank Olle Engkvists Stiftelse, Carl Tryggers Stiftelse for Vetenskaplig Forskning (CTS), and the Swedish Research Council (VR) for financial support. SNIC and HPC2N are acknowledged for providing the computing facilities.

https://dx.doi.org/10.1021/acs.inorgchem.0c00758
Inorg. Chem. XXXX, XXX, XXX−XXX

REFERENCES

(1) (a) Chen, X.; Yang, J.; Wu, T.; Li, L.; Luo, W.; Jiang, W.; Wang, L. Nanostructured binary copper chalcogenides: synthesis strategies and common applications. *Nanoscale* **2018**, *10*, 15130−15163. (b) Coughlan, C.; Ibanez, M.; Dobrozhan, O.; Singh, A.; Cabot, A.; Ryan, K. M. Compound copper chalcogenide nanocrystals. *Chem. Rev.* **2017**, *117*, 5865−6109.

(2) (a) Xue, J.; Liu, J.; Liu, Y.; Li, H.; Wang, Y.; Sun, D.; Wang, W.; Huang, L.; Tang, J. Recent advances in synthetic methods and applications of Ag_2S-based heterostructure photocatalysts. *J. Mater. Chem. C* **2019**, *7*, 3988−4003. (b) Gui, R.; Jin, H.; Wang, Z.; Tan, L. Recent advances in synthetic methods and applications of colloidal silver chalcogenide quantum dots. *Coord. Chem. Rev.* **2015**, *296*, 91−124.

(3) (a) Wang, X.; Qiu, P.; Zhang, T.; Ren, D.; Wu, L.; Shi, X.; Yang, J.; Chen, L. Compound defects and thermoelectric properties in ternary CuAgSe-based materials. *J. Mater. Chem. A* **2015**, *3*, 13662−13670. (b) Qiu, P. F.; Wang, X. B.; Zhang, T. S.; Shi, X.; Chen, L. D. Thermoelectric properties of Te-doped ternary CuAgSe compounds. *J. Mater. Chem. A* **2015**, *3*, 22454−22461.

(4) Han, C.; Sun, Q.; Cheng, Z. X.; Wang, J. L.; Li, Z.; Lu, G. Q.; Dou, S. X. Ambient scalable synthesis of surfactant-free thermoelectric CuAgSe nanoparticles with reversible metallic-*n*-*p* conductivity transition. *J. Am. Chem. Soc.* **2014**, *136*, 17626−17633.

(5) Gahlot, S.; Dappozze, F.; Singh, D.; Ahuja, R.; Cardenas, L.; Burel, L.; Amans, D.; Guillard, C.; Mishra, S. Room-temperature conversion of $Cu_{2-x}Se$ to CuAgSe nanoparticles to enhance photocatalytic performance of their composites with TiO_2. *Dalton Trans.* **2020**, *49*, 3580−3591.

(6) (a) Savory, C. N.; Ganose, A. M.; Travis, W.; Atri, R. S.; Palgrave, R. G.; Scanlon, D. O. An assessment of silver copper sulfides for photovoltaic applications: theoretical and experimental insights. *J. Mater. Chem. A* **2016**, *4*, 12648−12657. (b) Liu, Z.; Han, J.; Guo, K.; Zhang, X.; Hong, T. Jalpaite Ag_3CuS_2: A novel promising ternary sulfide absorber material for solar cells. *Chem. Commun.* **2015**, *51*, 2597−2600.

(7) Baker, C. L.; Lincoln, F. J.; Johnson, A. W. S. Crystal structure determination of Ag_3CuS_2 from powder X-Ray diffraction data. *Aust. J. Chem.* **1992**, *45*, 1441−1449.

(8) Mi, L.; Wei, W.; Zheng, Z.; Zhu, G.; Hou, H.; Chen, W.; Guan, X. Ag^+ insertion into 3D hierarchical rose-like $Cu_{1.8}Se$ nanocrystals with tunable band gap and morphology genetic. *Nanoscale* **2014**, *6*, 1124−1133.

(9) Bryks, W.; Smith, S. C.; Tao, A. R. Metallomesogen templates for shape control of metal selenide nanocrystals. *Chem. Mater.* **2017**, *29*, 3653−3662.

(10) Wang, Y.; Li, X.; Xu, M.; Wang, K.; Zhu, H.; Zhao, W.; Yan, J.; Zhang, Z. Pressure induced photoluminescence modulation in a wide range and synthesis of monodispersed ternary AgCuS nanocrystal based on Ag_2S nanocrystals. *Nanoscale* **2018**, *10*, 2577−2587.

(11) Brutchey, R. L. Diorganyl dichalcogenides as useful synthons for colloidal semiconductor nanocrystals. *Acc. Chem. Res.* **2015**, *48*, 2918−2926.

(12) Guo, Y.; Alvarado, S. R.; Barclay, J. D.; Vela, J. Shape-programmed nanofabrication: Understanding the reactivity of dichalcogenide precursors. *ACS Nano* **2013**, *7*, 3616−3626.

(13) Kisker, D. W.; Steigerwald, M. L.; Kometani, T. Y.; Jeffers, K. S. Low-temperature organometallic vapor phase epitaxial growth of CdTe using a new organotellurium source. *Appl. Phys. Lett.* **1987**, *50*, 1681−1683.

(14) Chu, J. Y. C.; Lewicki, J. W. Thermal decomposition of bis(diphenylmethyl) diselenide. *J. Org. Chem.* **1977**, *42*, 2491−2493.

(15) Chu, J. Y. C.; Marsh, D. G.; Günther, W. H. H. Photochemistry of organochalcogen compounds. I. Photolysis of benzyl diselenide. *J. Am. Chem. Soc.* **1975**, *97*, 4905−4908.

(16) (a) Shen, G.; Chen, M.; Guyot-Sionnest, P. Synthesis of nonaggregating HgTe colloidal quantum dots and the emergence of air-stable n-doping. *J. Phys. Chem. Lett.* **2017**, *8*, 2224−2228. (b) Zhou, B.; Li, M.; Wu, Y.; Yang, C.; Zhang, W.-H.; Li, C. Monodisperse $AgSbS_2$ nanocrystals: Size-control strategy, large-scale synthesis, and photoelectrochemistry. *Chem. - Eur. J.* **2015**, *21*, 11143−11151. (c) Zhang, J.; Gao, J.; Miller, E. M.; Luther, J. M.; Beard, M. C. Diffusion-controlled synthesis of PbS and PbSe quantum dots with in situ halide passivation for quantum dot solar cells. *ACS Nano* **2014**, *8*, 614−622.

(17) Chang, Y.-P.; Hector, A. L.; Levason, W.; Reid, G.; Whittam, J. Synthesis and properties of $MoCl_4$ complexes with thio- and seleno-ethers and their use for chemical vapour deposition of $MoSe_2$ and MoS_2 films. *Dalton Trans.* **2018**, *47*, 2406−2414.

(18) Gurnani, C.; Hawken, S. L.; Hector, A. L.; Huang, R.; Jura, M.; Levason, W.; Perkins, J.; Reid, G.; Stenning, G. B. G. Tin(IV) chalcogenoether complexes as single source precursors for the chemical vapour deposition of SnE_2 and SnE (E = S, Se) thin films. *Dalton Trans.* **2018**, *47*, 2628−2637.

(19) Chang, Y.-P.; Hector, A. L.; Levason, W.; Reid, G. Chalcogenoether complexes of Nb(V) thio- and seleno-halides as single source precursors for low pressure chemical vapour deposition of NbS_2 and $NbSe_2$ thin films. *Dalton Trans.* **2017**, *46*, 9824−9832.

(20) George, K.; de Groot, C. H.; Gurnani, C.; Hector, A. L.; Huang, R.; Jura, M.; Levason, W.; Reid, G. Telluroether and selenoether complexes as single source reagents for low pressure chemical vapor deposition of crystalline Ga_2Te_3 and Ga_2Se_3 thin films. *Chem. Mater.* **2013**, *25*, 1829−1836.

(21) Sparks, J. R.; He, R.; Healy, N.; Krishnamurthi, M.; Peacock, A. C.; Sazio, P. J. A.; Gopalan, V.; Badding, J. V. Zinc Selenide Optical Fibers. *Adv. Mater.* **2011**, *23*, 1647−1651.

(22) Boscher, N. D.; Carmalt, C. J.; Hyett, G.; Garcia Prieto, A.; Pankhurst, Q. A.; Parkin, I. P. Chromium oxyselenide solid solutions from the atmospheric pressure chemical vapour deposition of chromyl chloride and diethylselenide. *J. Mater. Chem.* **2008**, *18*, 1667−1673.

(23) Chang, Y.-P.; Levason, W.; Reid, G. Developments in the chemistry of the hard early metals (Groups 1−6) with thioether, selenoether and telluroether ligands. *Dalton Trans.* **2016**, *45*, 18393−18416.

(24) Kohyama, Y.; Murase, T.; Fujita, M. Control of silver(I)-dialkyl chalcogenide coordination by a synthetic cavity. *Angew. Chem., Int. Ed.* **2014**, *53*, 11510−11513.

(25) Levason, W.; Reid, G.; Zhang, W. The chemistry of the p-block elements with thioether, selenoether and telluroether ligands. *Dalton Trans.* **2011**, *40*, 8491−8506.

(26) Levason, W.; Orchard, S. D.; Reid, G. Recent developments in the chemistry of selenoethers and telluroethers. *Coord. Chem. Rev.* **2002**, *225*, 159−199.

(27) Gahlot, S.; Jeanneau, E.; Dappozze, F.; Guillard, C.; Mishra, S. Precursor-mediated synthesis of $Cu_{2-x}Se$ nanoparticles and their composites with TiO_2 for improved photocatalysis. *Dalton Trans.* **2018**, *47*, 8897−8905.

(28) Mishra, S.; Du, D.; Jeanneau, E.; Dappozze, F.; Guillard, C.; Zhang, J.; Daniele, S. A facile molecular precursor-based synthesis of Ag_2Se nanoparticles and its composites with TiO_2 for enhanced photocatalytic activity. *Chem. - Asian J.* **2016**, *11*, 1658−1663.

(29) Fang, C.; Zhang, S.; Zuo, P.; Wei, W.; Jin, B.; Wu, J.; Tian, Y. Nanotube−nanotube transformation synthesis and electrochemistry of crystalline CuAgSe nanotubes. *J. Cryst. Growth* **2009**, *311*, 2345−2351.

(30) Biesinger, M. C. Advanced analysis of copper X-ray photoelectron spectra. *Surf. Interface Anal.* **2017**, *49*, 1325−1334.

(31) Mishra, S.; Daniele, S. Metal-organic derivatives with fluorinated ligands as precursors for inorganic nanomaterials. *Chem. Rev.* **2015**, *115*, 8379−8448.

(32) Mishra, S.; Zhang, J.; Hubert-Pfalzgraf, L. G.; Luneau, D.; Jeanneau, E. The Interplay between yttrium, barium or copper trifluoroacetates and *N*-methyldiethanolamine: Synthesis of a heterometallic Y_3Cu trifluoroacetate complex and a homometallic Ba-TFA 1D polymer. *Eur. J. Inorg. Chem.* **2007**, *2007*, 602−608.

(33) Ayadi, H.; Fang, W.; Mishra, S.; Jeanneau, E.; Ledoux, G.; Zhang, J.; Daniele, S. Influence of Na^+ ion doping on the phase change and upconversion emissions of the GdF_3: Yb^{3+}, Tm^{3+} nanocrystals obtained from the designed molecular precursors. *RSC Adv.* **2015**, *5*, 100535−100545.

https://dx.doi.org/10.1021/acs.inorgchem.0c00758
Inorg. Chem. XXXX, XXX, XXX−XXX

(34) Mishra, S.; Jeanneau, E.; Bulin, A.-L.; Ledoux, G.; Jouguet, B.; Amans, D.; Belsky, A.; Daniele, S.; Dujardin, C. A molecular precursor approach to monodisperse scintillating CeF_3 nanocrystals. *Dalton Trans.* **2013**, *42*, 12633−12643.
(35) Mishra, S.; Jeanneau, E.; Daniele, S. Dimethyl selenide complexes of copper, gallium and indium halides as potential precursors for selenium-containing chalcopyrite semiconducting materials. *Polyhedron* **2010**, *29*, 500−506.
(36) Jura, M.; Levason, W.; Ratnani, R.; Reid, G.; Webster, M. Six- and eight-coordinate thio- and seleno-ether complexes of NbF_5 and some comparisons with $NbCl_5$ and $NbBr_5$ adducts. *Dalton Trans.* **2010**, *39*, 883−891.
(37) Lu, H.; Brutchey, R. L. Tunable room-temperature synthesis of coinage metal chalcogenide nanocrystals from N-heterocyclic carbene synthons. *Chem. Mater.* **2017**, *29*, 1396−1403.
(38) Fard, M. A.; Weigend, F.; Corrigan, J. F. Simple but effective: thermally stable Cu−$ESiMe_3$ *via* NHC ligation. *Chem. Commun.* **2015**, *51*, 8361−8364.
(39) Jones, A. C.; Hitchman, M. L. *Chemical vapour deposition: Precursors, processes and applications*; Royal Society of Chemistry, 2009.
(40) Mehlana, G.; Bourne, S. A. Unravelling chromism in metal−organic frameworks. *CrystEngComm* **2017**, *19*, 4238−4259.
(41) Setifi, F.; Benmansour, S.; Marchivie, M.; Dupouy, G.; Triki, S.; Sala-Pala, J.; Salaün, J.-Y.; Gomez-García, C. J.; Pillet, S.; Lecomte, C.; Ruiz, E. Thermochromism in a Molecular Cu^{II} Chain. *Inorg. Chem.* **2009**, *48*, 1269−1271.
(42) de Almeida, K. J.; Ramalho, T. C.; Rinkevicius, Z.; Vahtras, O.; Ågren, H.; Cesar, A. Theoretical study of specific solvent effects on the optical and magnetic properties of copper(II) acetylacetonate. *J. Phys. Chem. A* **2011**, *115*, 1331−1339.
(43) *CrysAlisPro Software System*; Rigaku Oxford Diffraction, 2018.
(44) Clark, R. C.; Reid, J. S. The analytical calculation of absorption in multifaceted crystals. *Acta Crystallogr., Sect. A: Found. Crystallogr.* **1995**, *51*, 887−897.
(45) Sheldrick, G. M. ShelXT-Integrated space-group and crystal-structure determination. *Acta Crystallogr., Sect. A: Found. Adv.* **2015**, *A71*, 3−8.
(46) Dolomanov, O. V.; Bourhis, L. J.; Gildea, R. J.; Howard, J. A. K.; Puschmann, H. Olex2: A complete structure solution, refinement and analysis program. *J. Appl. Crystallogr.* **2009**, *42*, 339−341.
(47) Sheldrick, G. M. Crystal structure refinement with ShelXL. *Acta Crystallogr., Sect. C: Struct. Chem.* **2015**, *71*, 3−8.
(48) Kresse, G.; Furthmüller, J. Efficient iterative schemes for ab initio total-energy calculations using a plane-wave basis set. *Phys. Rev. B: Condens. Matter Mater. Phys.* **1996**, *54*, 11169−11186.
(49) Kohn, W. Density functional and density matrix method scaling linearly with the number of atoms. *Phys. Rev. Lett.* **1996**, *76*, 3168−3171.
(50) Kohn, W.; Sham, L. J. Self-consistent equations including exchange and correlation effects. *Phys. Rev.* **1965**, *140*, A1133−A1138.
(51) Kresse, G.; Joubert, D. From ultrasoft pseudopotentials to the projector augmented-wave method. *Phys. Rev. B: Condens. Matter Mater. Phys.* **1999**, *59*, 1758−1775.
(52) Perdew, J. P.; Burke, K.; Ernzerhof, M. Generalized gradient approximation made simple. *Phys. Rev. Lett.* **1996**, *77*, 3865−3868.
(53) Monkhorst, H. J.; Pack, J. D. Special points for brillouin-zone integrations. *Phys. Rev. B* **1976**, *13*, 5188−5192.
(54) Majure, D. L.; Haskins, R. W.; Lee, N. J.; Ebeling, R. M.; Maier, R. S.; Marsh, C. P.; Bednar, A. J.; Kirgan, R. A.; Welch, C. R.; Cornwell, C. F. Large-scale atomic/molecular massively parallel simulator (LAMMPS) simulations of the effects of chirality and diameter on the pullout force in a carbon nanotube bundle. *2008 DoD HPCMP Users Group Conference*; IEEE, 2008; pp 201−207.
(55) Humphrey, W.; Dalke, A.; Schulten, K. VMD: Visual molecular dynamics. *J. Mol. Graphics* **1996**, *14*, 33−38.
(56) Stukowski, A. Visualization and analysis of atomistic simulation data with OVITO−the open visualization tool. *Modell. Simul. Mater. Sci. Eng.* **2010**, *18*, 015012.
(57) Melchionna, S.; Ciccotti, G.; Lee Holian, B. Hoover NPT dynamics for systems varying in shape and size. *Mol. Phys.* **1993**, *78*, 533−544.
(58) Tobias, D. J.; Martyna, G. J.; Klein, M. L. Molecular dynamics simulations of a protein in the canonical ensemble. *J. Phys. Chem.* **1993**, *97*, 12959−12966.
(59) Rappe, A. K.; Casewit, C. J.; Colwell, K. S.; Goddard, W. A.; Skiff, W. M. UFF, a full periodic table force field for molecular mechanics and molecular dynamics simulations. *J. Am. Chem. Soc.* **1992**, *114*, 10024−10035.
(60) Saravanan, S.; Balachandran, V. Quantum chemical studies, natural bond orbital analysis and thermodynamic function of 2, 5-dichlorophenylisocyanate. *Spectrochim. Acta, Part A* **2014**, *120*, 351−364.
(61) Singh, D.; Gupta, S. K.; Sonvane, Y.; Lukacevic, I. Antimonene: A monolayer material for ultraviolet optical nanodevices. *J. Mater. Chem. C* **2016**, *4*, 6386−6390.

https://dx.doi.org/10.1021/acs.inorgchem.0c00758
Inorg. Chem. XXXX, XXX, XXX−XXX